AD-A041 085 ARMY ELECTRONICS COMMAND FORT MONMOUTH N J F/G 4/1
LIDAR DETECTION OF SUBVISIBLE REENTRY VEHICLE EROSIVE ATMOSPHER--ETC(U)
MAR 77 R RUBIO
UNCLASSIFIED ECOM-5813 NL

1 OF 1
ADA
041085

END

DATE
FILMED
7-77

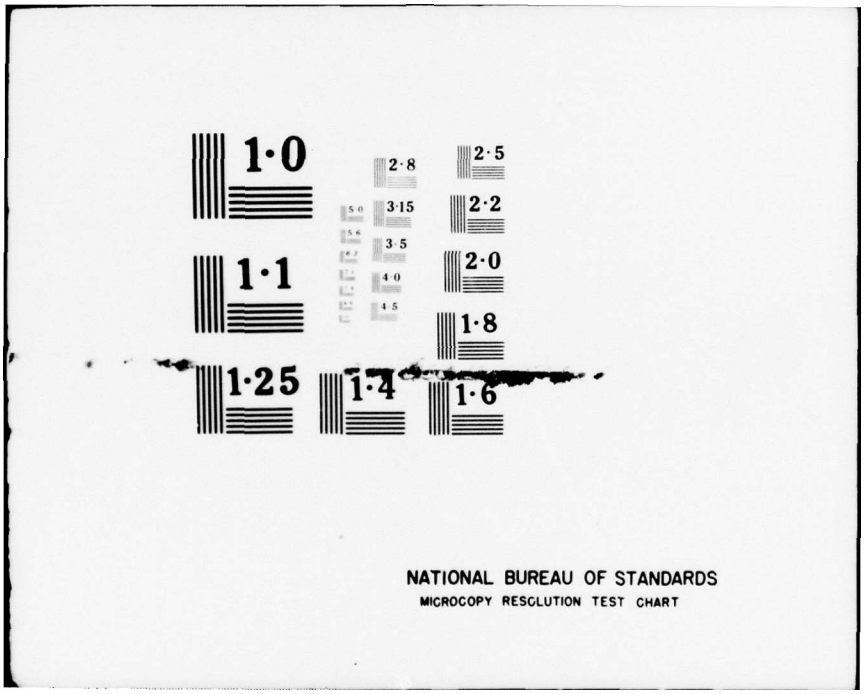
1·0
1·1
1·25
1·4
1·6
1·8
2·0
2·2
2·5
2·8
3·15
3·5
4·0
4·5
5·0
5·6
NATIONAL BUREAU OF STANDARDS
MICROCOPY RESOLUTION TEST CHART

AD

Reports Control Symbol
OSD-1366

RESEARCH AND DEVELOPMENT TECHNICAL REPORT
ECOM-5813

LIDAR DETECTION OF SUBVISIBLE REENTRY VEHICLE EROSIVE ATMOSPHERIC MATERIAL

By

ROBERTO RUBIO

Atmospheric Sciences Laboratory
US Army Electronics Command
White Sands Missile Range, New Mexico 88002

March 1977

Approved for public release; distribution unlimited.

ECOM

UNITED STATES ARMY ELECTRONICS COMMAND - FORT MONMOUTH, NEW JERSEY 07703

NOTICES

Disclaimers

The findings in this report are not to be construed as an official Department of the Army position, unless so designated by other authorized documents.

The citation of trade names and names of manufacturers in this report is not to be construed as official Government indorsement or approval of commercial products or services referenced herein.

Disposition

Destory this report when it is no longer needed. Do not return it to the originator.

SECURITY CLASSIFICATION OF THIS PAGE *(When Data Entered)*

REPORT DOCUMENTATION PAGE

READ INSTRUCTIONS BEFORE COMPLETING FORM

1. REPORT NUMBER: ECOM-5813	2. GOVT ACCESSION NO.
3. RECIPIENT'S CATALOG NUMBER	
4. TITLE *(and Subtitle)*: LIDAR DETECTION OF SUBVISIBLE REENTRY VEHICLE EROSIVE ATMOSPHERIC MATERIAL	5. TYPE OF REPORT & PERIOD COVERED
	6. PERFORMING ORG. REPORT NUMBER
7. AUTHOR(s): Roberto Rubio	8. CONTRACT OR GRANT NUMBER(s)
9. PERFORMING ORGANIZATION NAME AND ADDRESS: Atmospheric Sciences Laboratory, White Sands Missile Range, New Mexico 88002	10. PROGRAM ELEMENT, PROJECT, TASK AREA & WORK UNIT NUMBERS: DA Task No. 1L161102B53A
11. CONTROLLING OFFICE NAME AND ADDRESS: US Army Electronics Command, Fort Monmouth, New Jersey 07703	12. REPORT DATE: March 1977
	13. NUMBER OF PAGES: 35
14. MONITORING AGENCY NAME & ADDRESS *(if different from Controlling Office)*	15. SECURITY CLASS. *(of this report)*: UNCLASSIFIED
	15a. DECLASSIFICATION/DOWNGRADING SCHEDULE

16. DISTRIBUTION STATEMENT *(of this Report)*

Approved for public release; distribution unlimited

17. DISTRIBUTION STATEMENT *(of the abstract entered in Block 20, if different from Report)*

18. SUPPLEMENTARY NOTES

19. KEY WORDS *(Continue on reverse side if necessary and identify by block number)*

Reentry
Ablation
Atmospheric layer
Subvisible
Lidar

20. ABSTRACT *(Continue on reverse side if necessary and identify by block number)*

This report describes a lidar technique employed to detect conventionally undiscernible atmospheric particulate concentrations which cause unexpected nose-cone erosions of reentry missiles. It also describes the experiment, data, and data analysis results obtained during several Athena-H reentry missions conducted at White Sands Missile Range, New Mexico. Lidar data recorded on the Athena-H reentry nights of 26 April and 24 August 1973 provided information on subvisible tenuous layers located at heights of 9.3 km and 14.3 km, respectively. Analysis of the lidar data, concurrently recorded radiosonde meteorological data, and a

DD FORM 1 JAN 73 1473 EDITION OF 1 NOV 65 IS OBSOLETE

SECURITY CLASSIFICATION OF THIS PAGE *(When Data Entered)*

20. Abstract (cont)

clear day aerosol model yielded an average volume backscattering coefficient of 4.3 x 10^{-5}/m for the 9.3 km layer which was 310 m thick and 3.2 x 10^{-5}/m for the 14.3 km layer which was 500 m in depth. Calculations based on previous in-situ measurements of particulate sizes and elemental composition yielded an average concentration of 3.7 x 10^{5} liquid droplets/m^3 or 2.6 x 10^{4} ice crystals/m^3 for the 26 April cloud striation and an average concentration of 2 x 10^{4} ice particles/m^3 or 2.2 x 10^{8} arid particles/m^3 for the 24 August layer. The lidar data clearly distinguished between a truly clear atmospheric path, 21 March, and an apparently clear atmospheric path, 26 April and 24 August.

CONTENTS

	Page
INTRODUCTION	2
ATMOSPHERIC LAYER DETECTION THEORY	2
LIDAR SYSTEM	6
ATMOSPHERIC PROBING RESULTS	9
IMMEDIATE DATA	14
DATA ANALYSIS RESULTS	14
CONCLUSIONS	22
REFERENCES	24

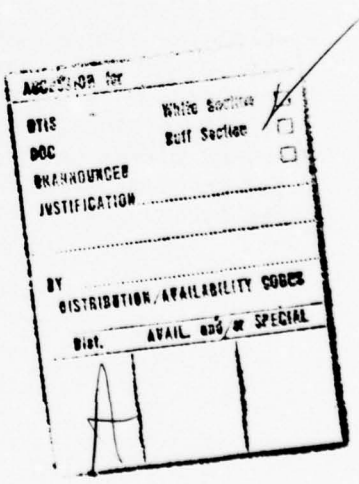

INTRODUCTION

Missile reentry flight tests have demonstrated that high-velocity traversal of rain or clouds causes extensive damage to reentry thermal protective material [1]. Since an ablating nose cone with a small angle of attack will erode asymmetrically, excessive ablation will alter significantly the reentry projectile's angle of attack. The problem is compounded by the fact that these asymmetrical ablations have been observed during flights through an atmosphere classified as "clear" [2]. As an effort to identify the cause of excessive ablation during clear sky conditions, the United States Air Force Space and Missile System Organization and the US Army Atmospheric Sciences Laboratory jointly sponsored the research effort described here. Although atmospheric ablation of reentry vehicles is a function of heat shield material, body geometry, angle of attack, and atmospheric density, this report is solely related to the detection of subvisible atmospheric material which apparently introduced nose-cone erosion beyond which would be normally observed or calculated based upon rocketsonde atmospheric density data.

Specifically, this report describes the laser light detection and ranging (lidar) technique used to locate visually unobservable atmospheric particulate concentrations during several Athena-H flights which originated at Green River, Utah, and impacted at White Sands Missile Range, New Mexico. Subvisible tenuous atmospheric layers were located with the lidar system and their spatial extent was measured at altitudes of interest along the anticipated reentry trajectory. This study shows that lidar data not only serves to identify the existence of invisible layers and their heights and thicknesses, but also provides measurements which when analyzed in conjunction with radiosonde meteorological data and an aerosol model can contribute plausible information on the particle identity and average concentration.

ATMOSPHERIC LAYER DETECTION THEORY

Lidar transmitter emissions are electromagnetic wave pulses at optical wavelengths with a high monochromatic quality. At optical wavelengths, these pulses, while propagating through the atmosphere, interact with atmospheric molecules and particulates and produce a backscattered laser light signal of sufficient magnitude to be detectable by a receiver mirror and photomultiplier arrangement. The fraction of the total backscattered light power collected by the receiver mirror is given by Eq. (1).

$$P_i(r) = \frac{E_t cA}{8\pi r^2} [\beta\rho(r) + Bn(r) + \Gamma m(r)] e^{-2\int_0^r (\alpha + \gamma + \sigma)dr} \qquad (1)$$

where

P_i = power incident on receiver aperture.

E_t = transmitted laser energy.

A = receiver aperture.

B = average aerosol backscattering cross-sectional area.

Γ = cloud particles average backscattering cross-sectional area.

r = slant range.

c = speed of light.

m = cloud-average particle density.

n = aerosol average density.

α = molecular extinction coefficient.

β = Rayleigh backscattering cross-sectional area.

γ = aerosol extinction coefficient.

ρ = molecular density.

σ = cloud extinction coefficient.

The quantity of importance here is the cloud volume backscattering coefficient, $\Gamma m(r)$. Even though cloud water droplet concentrations, $n(r)$, are minor in numbers when compared to the molecular densities, $\rho(r)$, their particulate sizes are comparable to or greater than the laser wavelength, and thus their backscattering efficiency is much greater than that of molecules. It is this effect which renders a lidar useful for detection of subvisible tenuous layers. Thin, high-altitude clouds, which are normally the type of unobservable clouds present during reentry mission, have empirically been determined to be adequately characterized as predominantly single scattering ensembles [3]. Thus, in Eq. (1), the term $\Gamma m(r)$ is that for a tenuous cloud in which multiple scattering effects are negligible; i.e., $\sigma < 0.1$.

An example of lidar data manifesting a subvisible cloud on a clear day is shown in Figure 1. Depicted on the left side of this oscilloscope photograph is a trace representative of the magnitude of the recorded atmospherically backscattered laser energy as a function of altitude. The right side pulse is the output of a photodiode which senses a fraction of the laser's output energy. The second grid from the bottom on the left trace of Figure 1 shows the pulse caused by the cloud reflections. This cloud was at a height of 3.5 km above ground level (AGL). The assertion that this pulse represents a subvisible cloud is based on studies of several photograph sets of laser energy reflections from visible striated clouds which gradually disappeared to the human eye but remained detectable with the lidar system.

Particulate concentrations (clouds) may be composed of water clustered hygroscopic nuclei [4] or anhydrous particulate matter such as dust layers [5]. Either concentration will enhance the magnitude of the expression $\Gamma m(r)$ and introduce amplitude variations in the reflected laser energy profile. The data of Figure 2, also obtained on a totally clear day, show energy trace undulations which are not uncommon at tropospheric altitudes and are the result of particulate stratifications. Mathematically, the amplitude variations represent changes in the quantity $\Gamma m(r)$ which describes the backscattering properties of the particulate layer. Unlike the case shown in Figure 1, there is normally no prior information regarding the particulate size or composition of a lidar detected subvisible layer. Nonetheless, based on past in-situ microstructure measurements of high-altitude layers, reasonable average particle sizes were assumed to obtain average particle density.

In the absence of clouds [$m(r) = 0$] and a sufficiently dispersed aerosol medium [$n(r)$, small], the backscattered energy amplitude is proportional to the sum of the quantities $\beta\rho(r)$ and $Bn(r)$ and appears as a smooth trace on the osciiloscope data photograph. Figure 3 is a data film of a smooth energy profile recorded along an exceptionally clear atmospheric path, 21 March 1973, with visibility greater than 60 km. The atmosphere was devoid of any particulate layers on that morning.

The other expression in Eq. (1) containing atmospheric constituent factors is the exponential quantity $\exp -2\left[\int(\alpha + \gamma + \sigma)dr\right]$ which represents the atmospheric attenuation of the laser beam intensity as a function of range. Because of the rarefied character of the subvisible layers, no attempt was made to extract any specific atmospheric particle information from this exponential coefficient.

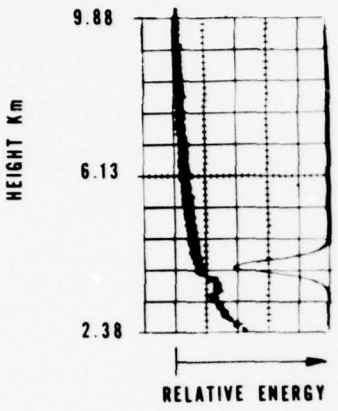

Figure 1. Lidar height and relative backscattered energy profile (left trace). Note pulse at 3.5 km caused by tenuous cloud.

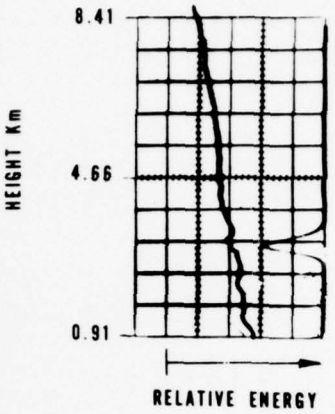

Figure 2. Backscattered laser energy undulations caused by thin particulate layers.

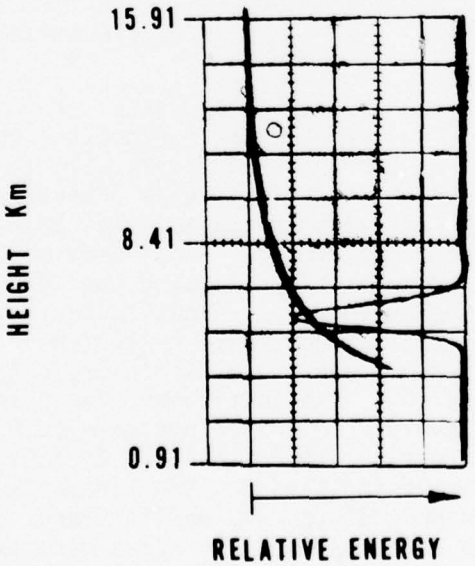

Figure 3. Profile of backscattered laser energy on a day devoid of clouds and particulate layers.

LIDAR SYSTEM

The Sandia Laboratory GB-60B lidar system, shown in Figure 4, was employed during the Athena-H reentry projects. This system consists primarily of a "Q-switched" ruby laser transmitter, a Cassegrainian telescope, light filter, and a photomultiplier comprising the receiver, an ME-16 tracking mount with sighting telescopes, and the electronic systems for digital ranging and data recording. Landry and Lockner [6] describe the GB-60B lidar and associated instrumentation in detail. The basic lidar characteristics are as follows:

Wavelength	6943 angstroms
Maximum output energy	4 joules/pulse (Q-spoiled)
Pulse width	20-30 nanoseconds
Maximum beam divergence	8.5 milliradians
Maximum repetition rate	20 per minute
Light filter bandwidth	20 angstroms
Receiver aperture	1.68 square meters
Photomultiplier	RCA 7265
Sighting capability	Azimuth 0 to 360 degrees Elevation 0 to 90 degrees

Transmitted laser energy, E_t, per pulse was determined from the photocathode pulses (like those shown in Figures 1 through 3 on the right side trace) and an energy output calibration. It was established that the area under each of these pulses is proportional to the amount of laser energy which activated the photodiode, provided that the photodiode is a linear detector [7]. A calibration curve was constructed before each probing mission by plotting photodiode pulse area as a function of laser output energy. Output energy levels were set by adjusting the laser flashlamp voltage. A light-beam splitter, situated between the laser rod front end and a Hadron conical aperture thermopile, deflects approximately 4% of the total beam energy into an ITT F4000 photodiode. Energy levels were maintained between 0.5 joule/pulse and 2.5 joules/pulse in order to stay within the detector's linear region. During the atmospheric lasing periods, the thermopile was removed, but the beam splitter and photodiode remained in place. Photographs of oscilloscope displays of the photodiode pulse were subsequently used in conjunction with the calibration to establish the individual pulse energy.

Figure 4. GB-60B laser light ranging and detection system.

Atmospherically reflected laser energy collected by the receiver's primary mirror is focused, via a secondary mirror and a glass enclosed light filter, onto the photomultipliers photoemissive surface. The corresponding photomultiplier output signals are fed directly to an oscilloscope where the voltage amplitudes are displayed and photographed. When the sampling time, Δt, is greater than the emitted pulse width, τ, and the voltage amplitude remains approximately constant within Δt, the light power incident on the primary mirror may be obtained from the recorded voltage by employing the relation:

$$P_i = \frac{\nu}{R_i R_\lambda g N_o} \tag{2}$$

where

ν = oscilloscope voltage.

g = photomultiplier gain.

R_i = oscilloscope input impedance.

R_λ = photomultiplier responsivity at a specific wavelength.

N_o = receiver optical attenuation.

Voltage samples used in this experiment were 0.1μsec long, 3.3 times longer than the maximum pulse width and sufficiently short to maintain the backscattered energy relatively constant.

Solution of Eq. (2) requires a knowledge of the lidar system parameters R_i, R_λ, g, and N_o. By terminating the photomultiplier output cable with a fixed resistor load, the oscilloscope input impedance R_i, was maintained at 50 ohms. A responsivity of $R_\lambda = 16 \times 10^{-3}$ amps/watt as listed in the tube specifications for ruby wavelength was assumed since a new RCA 7265 photomultiplier was installed specifically for the Athena projects. Photomultiplier gains, g, are different for each tube configuration, dynode circuitry, and applied anode-to-cathode voltage. While the tube configuration and dynode circuitry remain fixed during a test, the anode voltage does not; therefore, a gain versus anode voltage table had to be established. The measured gains, g, as a function of applied voltage are listed below:

Anode Voltage (kV)	Photomultiplier Gain
1.3	1.4×10^3
1.4	3.1×10^3
1.5	6.6×10^3
1.6	1.3×10^4
1.7	2.6×10^4
1.8	4.8×10^4
1.9	8.7×10^4
2.0	1.6×10^5
2.1	2.6×10^5
2.2	4.4×10^5
2.3	7.6×10^5
2.4	1.0×10^6

The receiver optical attenuation factor, N_o, accounts for mirror reflection losses and the light filter and its glass enclosure losses. To determine the system's optical attenuation, radiation from a standard tungsten ribbon lamp was directed onto the photomultiplier, and its output current was measured. Subsequently, a current reading was obtained after the same radiation was allowed to pass through the mirrors, filter, and glass enclosures. Irradiation was at a wavelength of 0.7 angstrom. A value of 0.36 was obtained from the ratio of the two output currents and the respective aperture areas. This value was then multiplied by 0.9, the photomultiplier glass enclosure transmissivity, to establish N_o to be 0.32.

The slant range of each specific target is also acquired from the oscilloscope photograph. Fixed time delay gating of the scope's horizontal sweep trigger and the subsequent elapsed times read from the data poloroid prints provide the total pulse travel time required to calculate the reflection range.

ATMOSPHERIC PROBING RESULTS

The principal lidar objective was to detect material concentrations normally undiscernible by conventional techniques which might be present at the specific heights of 12 and 6 km along the reentry path. A secondary objective was to establish whether subvisible particulate layers existed at any altitude and, if so, determine the layer altitude and depth. The GB-60B lidar and peripheral equipment were located at the White Sands Small Missile Range, 40 km south of the programmed Athena-H impact area. Figure 5 shows the lidar's geographical location and three eliptical areas denoting the locations of the atmospheric regions where the anticipated Athena-H trajectory intersects the 12 km, 6 km,

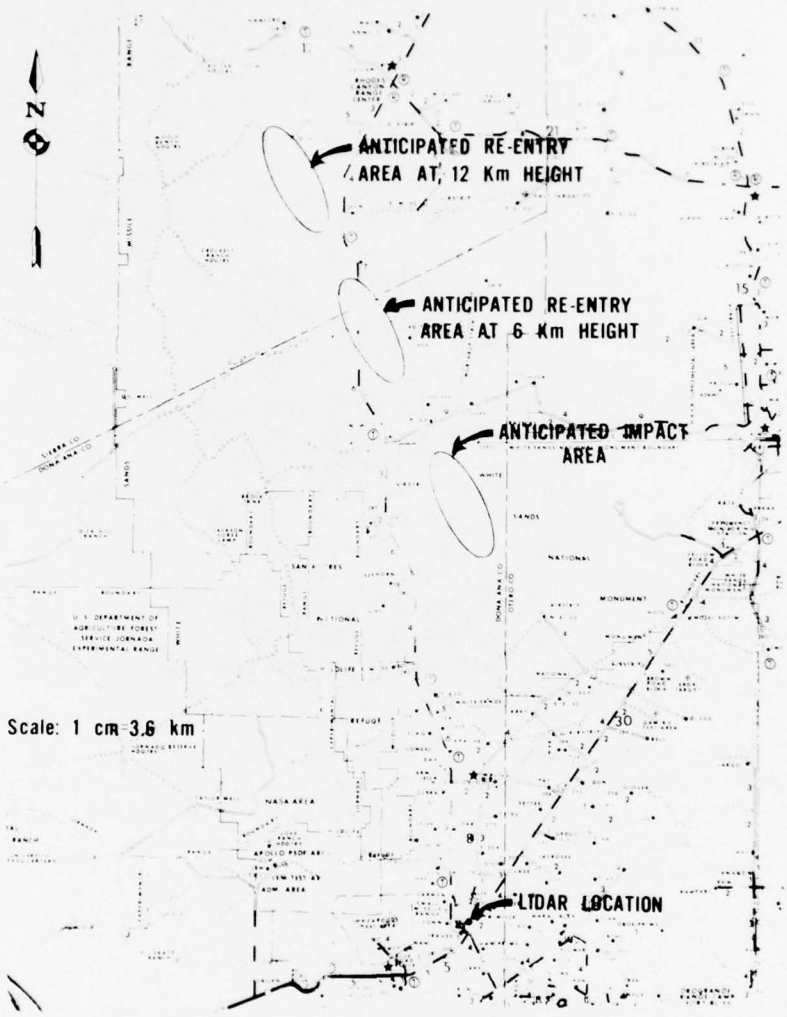

Figure 5. Map denoting lidar location and Athena-H atmospheric reentry areas probed.

and surface levels. Since the atmospheric volumes centered at the 12 and 6 km intersection were the regions of primary concern, most of the laser probing was directed towards these areas while other altitude intervals along the reentry path were probed only intermittently.

Seven Athena-H reentry missions were supported: four missiles were successfully launched and three were aborted due to either excessively high wind velocities at the launch site or excessive cloud coverage at the missile impact area. Laser probing served not only to detect visually imperceptible layers but also to provide weather personnel with cloud coverage information. On the afternoon of the first Athena cancellation, the sky cloud coverage was approximately 75% with a preponderance of cumulus clouds. Later in the evening and during the night, sky coverage increased with cirrus clouds covering most of the sky's open spaces. Examples of laser energy reflections from a cumulus cloud, recorded at 1459 MST, and a cirrus cloud, recorded at 2115, both on 22 March 1973, are shown in Figures 6 and 7, respectively. Layers of sporadically occurring and faintly observable cirrus type clouds, centered at a height of about 4.8 km, were detected on 29 March 1973 when two Athena-H missiles impacted on Small Missile Range.

On the night of 26 April 1973, an Athena-H missile reentered through an over-the-impact-area cloud coverage, described earlier in the day as less than one-tenth by a meteorological observer. Continual recordings of laser energy reflections from these clouds made possible their identification as water clouds which persisted during the night when they were visually unobservable. Figure 8 shows the voltage enhancement, at 9.3 km, caused by these subvisible tenuous water layers. Elsewhere, the atmosphere was found devoid of any particulate layers up to an altitude of 30 km on this day.

During the night of 23-24 August 1973, the laser was successfully employed to detect an otherwise invisible atmospheric particulate layer at a height of 14.3 km. In addition, at the low altitudes of 0.5 and 1.5 km, thin particulate concentrations were also displayed in the laser returned signals (Figure 9a). Further laser probing results showed the regions between 1.5 and 13.5 km, and above 15 km, to be clear of aerosol layers. Figures 9b and 9c show two atmospherically clear regions which were of interest to the Athena project. The visually imperceptible layer in Figure 9d, located at a height of 14.3 km, is 0.5 km in depth. This layer prevailed throughout the Athena flight time.

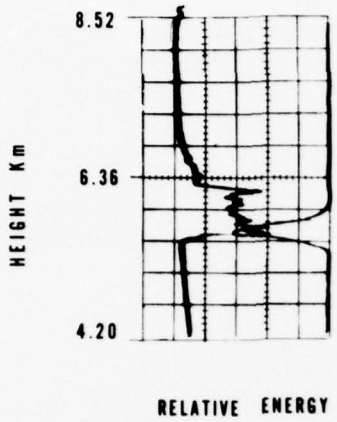

Figure 6. Voltage enhancement caused by visible cumulus cloud at a height of 5.9 km.

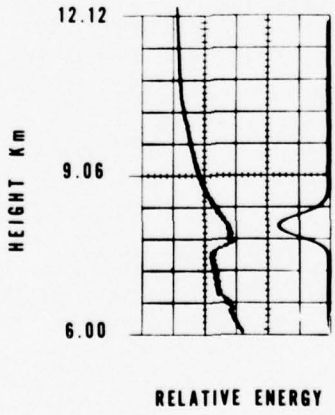

Figure 7. Voltage enhancement caused by observable cirrus cloud at a height of 7.8 km.

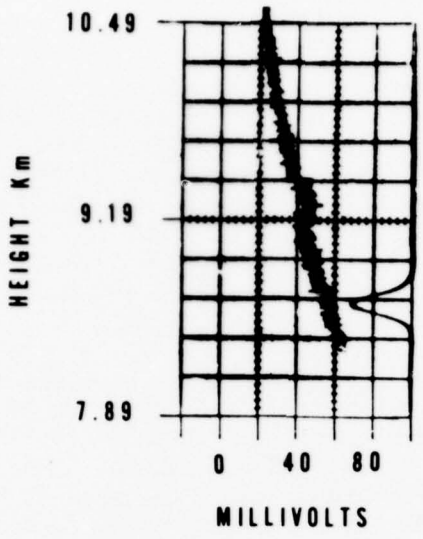

Figure 8. Voltage enhancement, proportional to backscattered laser energy, at 9.3 km caused by a subvisible cloud.

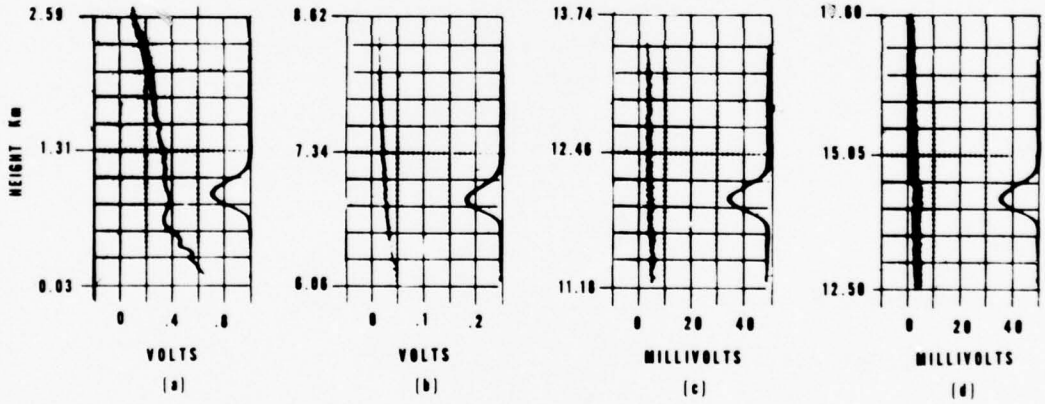

Figure 9. Reflected laser energy profiles which show the status of different regions of the atmosphere immediately after Athena-entry 24 August 1973:

(a) Low-level, thin layer particulate concentrations.
(b) Clear atmosphere at 6 km height.
(c) Clear atmosphere at 12 km height.
(d) High-altitude, subvisible particulate layer. Lidar beam azimuth and elevation were 347° and 20°, respectively.

IMMEDIATE DATA

Atmospherically induced enhancement of backscattered laser light intensity provides immediate information relative to the existence, range, and thickness of subvisible particulate layers. When a layer was detected, its horizontal spatial extent out to the region of interest was easily measured. For example, Figure 10 depicts the measured forward horizontal extent of the subvisible layer shown in Figure 9d. Its extent was established by varying the laser beam elevation angle from 90° to 10°. The azimuthal direction of the beam was 347°, which coincided with the anticipated reentry path.

Layer depths were determined simply by multiplying the time duration of the voltage enhancement by one-half of the magnitude of the speed of light and the sine of the laser beam elevation angle. Again, referring to the layer in Figure 9d, its vertical depth was immediately found to be 500 m at a point 72 km forward of the lidar system. The tenuous cloud of 26 April (Figure 8) was also immediately calculated to have a vertical depth of 360 m at that geographical location.

DATA ANALYSIS RESULTS

The laser backscattered energy data were further analyzed to determine the approximate microstructure characteristics of each particulate layer. Balloon radiosonde meteorological data and an aerosol model [8] were used to complete the solution of Eq. (1). To obtain average ice particle or water droplet densities, Eq. (1) is expressed in terms of the mean cloud volume backscattering coefficient:

$$\Gamma m = \frac{8\pi}{E_t A c} \frac{P_i(r) r^2}{T_a^2(r) T_\rho^2(r)} \tag{3}$$

where

Γ = average backscattering cross-sectional area.

m = average particle density.

$$T_a^2(r) = e^{-2\int \gamma(r)dr} \tag{3a}$$

$$T_\rho^2(r) = T_{\rho s}^2(r) \times T_{\rho a}^2(r) \tag{3b}$$

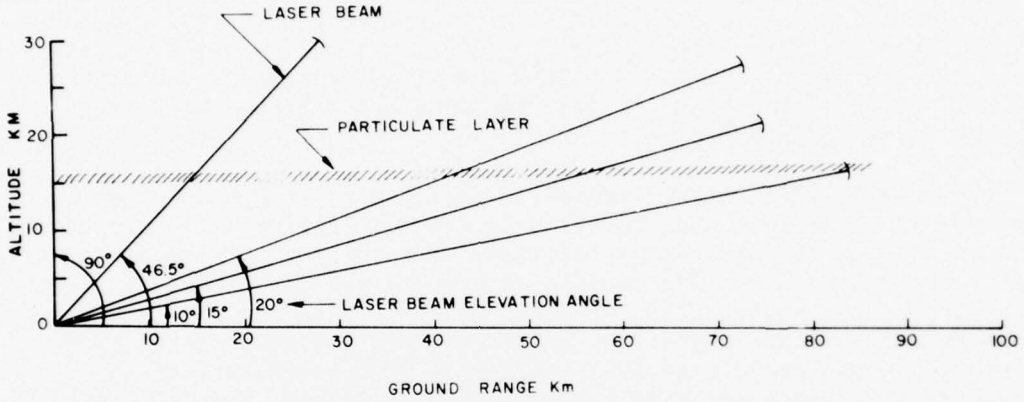

Figure 10. Forward geographical extent of subvisible particulate ensemble detected on 24 August 1973.

$$T^2_{\rho s} = e^{-2\int \alpha_1(r)dr} \tag{3c}$$

$$T^2_{\rho a} = e^{-2\int \alpha_2(r)dr} \tag{3d}$$

where

α_1 = molecular scattering coefficient.

α_2 = molecular absorption coefficient.

In this solution of Eq. (1), $\beta\rho(r)$ and Bn(r) were considered to be zero within the layer since the predominant backscattered energy from the cloud layer is that energy which is reflected from the water particles. Also because of the limited vertical extent and suspected low particle concentration of the cloud layer, the cloud extinction coefficient [$\sigma < 0.1$] was considered negligible.

At ruby wavelengths, electromagnetic wave absorption by atmospheric aerosol is negligible when compared to aerosol scattering. Molecular absorption, on the other hand, was considered because of the atmospheric water absorption bands [9] located within the emitted bandwidth. Temperature measurements of the GB-60B ruby rod, which was constantly cooled with an alcohol-water solution, indicated that lasing occurred at an average rod temperature of 2°C. Lasing at 2°C causes the emission linewidth to be 5 angstroms wide [10]. Consequently, the emitted laser spectrum ranged from 6939 to 6944 angstroms. Within this spectrum lie six narrow water vapor absorption lines, each of which is about 0.25 angstrom wide. To account for water vapor absorption, relative humidity data recorded by radiosonde instruments used in support of each reentry mission were integrated into centimeters of precipitable water. Based upon the computed integrated water mass value, the transmittance at 0.69 micron was obtained from the water vapor transmittance chart compiled by McClatchey [8].

Laser beam attenuation by the dispersed atmospheric aerosol background existing between the laser and the layer base was approximated by utilizing the McClatchey aerosol model. Corrections for attenuation due to molecular scattering were based on atmospheric density values obtained from radiosonde data. Radiosonde atmospheric density data from ground level to the layer base were converted to number of particles per unit volume, averaged over 1/2 km intervals, multiplied by the scattering cross-sectional area per molecule of $1.71 \times 10^{-3} m^2$ [11], and used to obtain the molecular optical thickness.

ERRATA PAGE FOR ECOM-5813

LIDAR DETECTION OF SUBVISIBLE REENTRY
VEHICLE EROSIVE ATMOSPHERIC MATERIAL

Page 16, last paragraph, next to last line in paragraph

Change $1.71 \times 10^{-3} m^2$ to 1.71×10^{-31}

Page 22, eleventh line from top of page

Change 0.1 to 0.1μ

Before the more detailed analysis of the laser data was performed, a determination, or at least a reasonable assumption, had to be made as to whether a detected layer was composed of either moist particles or anhydrous aerosols, since their respective electromagnetic energy scattering properties differ considerably. In certain cases where a layer was established beforehand as a water cloud, meteorological radiosonde data were used to determine if the cloud was composed solely of ice crystals. Mason [12] has reported that at temperatures of -70°C or less no supercooled water can exist in the liquid phase. Above 0°C, a totally liquid phase may be inferred. For temperatures between 0°C and -70°C, at least two sets of calculations were required: one representative of a liquid cloud and the other of an ice crystal cloud. For a mixture of liquid and ice particles, a third procedure, explained later, may be explored. When no advance information existed regarding the nature of the layer, an additional set of calculations was included to consider the existence of an anhydrous aerosol layer.

Analysis was first performed on the layer data shown on Figure 8 and recorded the night of the 26 April 1973 Athena-H mission. Although this was the third flight of the lidar support series, it was the first mission firing during which a subvisible layer occurred. A priori information revealed that the subvisible layer was a water cloud. This conclusion was based on daylight visual observations, concurrent lidar detection, and a continual lidar monitoring of the cloud until darkness when it was visually imperceptible. Examination of the radiosonde temperature data for 26 April 1973, 2130 MST, showed the atmospheric temperature to be -50.1°C at the cloud height of 9.3 km AGL. Therefore, the constituents in this cloud were one of the following three: all ice crystals, all supercooled liquid droplets, or a mixture of both. First, this cloud ensemble will be assumed as containing liquid droplets only. Subsequently, the cases of ice crystals only and a mixture of ice and liquid particles will be considered.

Computations of each of the Eq. (3) parameters pertaining to the laser cloud data of Figure 8 follow. The three transmittance factors were considered first. Based on the 2130 MST radiosonde relative humidity and temperature profiles, an integrated water mass quantity of 6.1 gm/cm^2 was obtained for the one-way laser beam slant path of 1058 km. A transmittance factor [$T^2_{\rho a}$] of 0.88 was obtained for two-way transmission over 6.1 gm/cm^2 of water. Calculation of the aerosol scattering factor [T^2_a] was based on the clear-day aerosol model data [8] over the same slant path distance from the lidar to the cloud base. A value of $T^2_a = 0.646$ was obtained. To evaluate Rayleigh scattering attenuation, radiosonde atmospheric density data for 26 April was employed. $T^2_{\rho s}$ was found to be 0.947.

Computation of the parameter, P_i, reflected light power incident on the primary mirror, required that first an averaging technique be developed for P_i, since it varies as a function of cloud depth due to the variations in range, particle size, and particle concentrations within the cloud. P_i values as a function of cloud depth were obtained from Eq. (2) and the voltages of Figure 8 which are shown replotted on Figure 11a. Subsequently computed range corrected P_i values, or $P_i r^2$, are shown in Figure 11b. The range corrected $\bar{P}$ (average value of 7.87×10^2 watt-m^2 was acquired from the equation

$$\bar{P} = \frac{\int_0^d P_{rc}(r)dr}{\int_0^d dr} \qquad (4)$$

where

P_{rc} = range corrected P_i values.

d = cloud depth in laser beam direction.

Laser output energy, E_t, corresponding to the pulse of Figure 8 (right side trace) was determined to be 1.7 joules. The photomultiplier gain at this time was 2.6×10^4.

Substitution of all the above numerical values into Eq. (3) yielded an average volume backscattering coefficient [Γm] of 4.3×10^{-5}/m. Since the base of this cloud was well above 6 km, the inference was that this was a cirrus cloud [13]. Such tenuous clouds are frequently visible over the White Sands basin during daylight hours but become subvisible at night. The predominant radius in cirrus type cloud particles is 4.2μm [4]. Using 4.2μm as the average water droplet radius, an index of refraction of 1.33, a mean backscattering cross-sectional area [Γ] of $1.1 \times 10^{-10}m^2$/particle was obtained. Employing this value and the above volume backscattering coefficient, an average water droplet concentration of approximately 3.8×10^5 particles/m^3 was finally established for the case of a liquid water cloud represented by Figure 8.

At an atmospheric temperature of -50.1°C it may be more reasonably assumed that the cloud layer was predominantly composed of ice crystals. Crystals in cirrus clouds are of columnar form [13]. It has also been shown that these columnar ice crystals are primarily in the size range of 8 to 50μm long with prism base radii 1/3 or smaller than their lengths [15] at temperatures of -50°C or less. Exact scattering cross-sectional areas for prismatic columns do not exist because of the mathematical intractabilities that have been encountered. Nevertheless, an

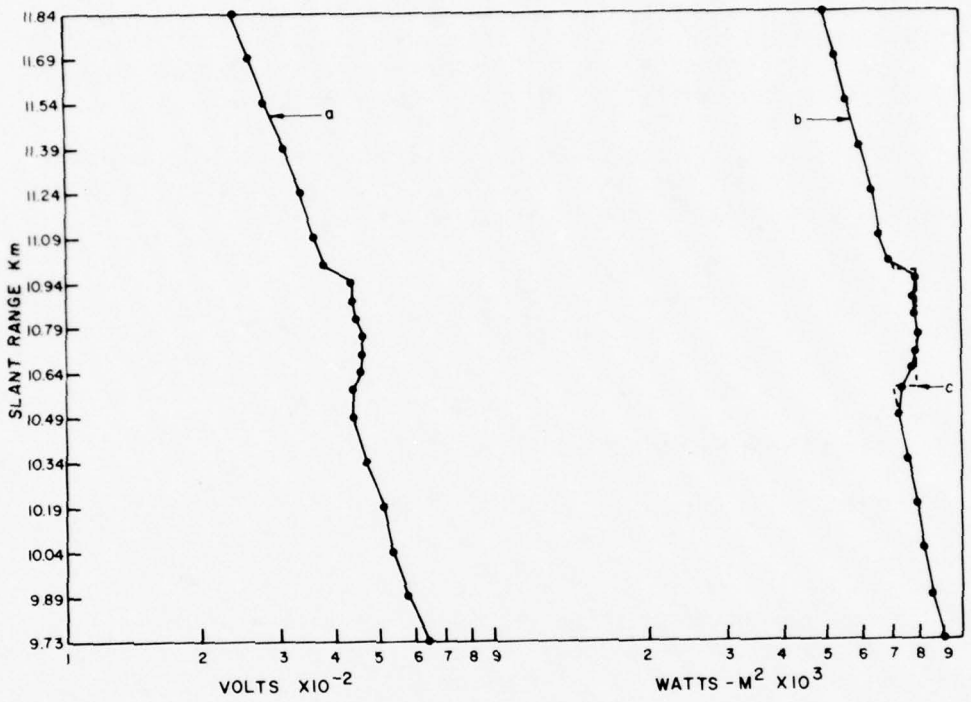

Figure 11. a. Lidar oscilloscope recorded voltage as function of slant range
b. Range corrected recorded power as a function of slant range.
c. Average range corrected power within cloud volume.

expression does exist for the scattering cross-sectional area of randomly oriented cylindrical ice crystals for which the crystal length, l, is $l > 2a > \lambda$; a is the crystal base radius, and λ is the wavelength of the incident wave [16]. This expression serves as a reasonable approximation for the backscattering cross-sectional area of a prismatic crystal. Employing the equation given in [16] and a Mie equivalent radius of 25μm, a backscattering cross-sectional area of $1.6 \times 10^{-9} m^2$ per crystal was obtained. Dividing this value into the volume backscattering coefficient of $4.3 \times 10^{-5}/m$ yielded an average ice crystal density of 2.7×10^4 crystal/m^3 for the cloud of Figure 8.

In the general case when the cloud composition consists of a mixture of liquid droplets and ice crystals, the respective particle concentrations would be deduced from an equation of the form

$$G = \overline{\Gamma}_{\ell} m_{\ell} + \overline{\Gamma}_{i} m_{i}$$

where

G = total volume backscattering coefficient.

l = liquid.

i = ice.

A simultaneous measurement of the liquid to ice particle concentration ratio is required to solve Eq. (4). Lidars with polarization discrimnation filters can provide this information [17]. The GB-GOB lidar did not have this capability during the Athena-H reentry flights; consequently, the above general equation cannot be solved here. However, trial combinations of fractions of the liquid and ice particles concentrations satisfying Eq. (4) may be employed until an answer is acquired which is representative of the excessive erosion encountered by the reentry projectile in question.

On 26 April 1973, the Athena-H reentry angle at the cloud height of 9.3 km AGL was -23°, the cloud depth in this reentry vicinity was 310 m. Therefore, from this lidar data it was calculated that the missile, which was traveling at approximately 6000 m/s, traversed through about 800 m of 3.7×10^5 liquid droplets/m^3, or 2.6×10^4 ice crystals/m^3, or a combination thereof. This was all erosive material which was unexpectedly present in an apparently clear atmosphere.

Normally, no a priori information is available about subvisible layers as was the case during the 24 August 1974 reentry flight. On that day the layer shown in Figure 9d, was lidar detected throughout mission support time at an average height of 14.3 km AGL. Examination of radiosonde data for the night of 23-24 August indicated atmospheric temperatures at the layer center varied from -70.3° to -72.6°C during the probing time interval. Therefore, it was concluded that this ensemble contained no water in the liquid phase and was thus composed of either ice crystals or anhydrous aerosols. Assuming that the layer particulates were all in the ice phase and the cloud was cirrus, because of its high-altitude location, the computational procedure followed in previous sections was repeated to again obtain the average microstructure cloud characteristics. Thereafter, the same analysis was performed under the assumption that the atmospheric stratification was composed solely of anhydrous aerosols.

To probe the reentry vicinity at a height of 14.3 km, lasing was conducted at an elevation angle of 20°, and thus a slant path of 41 km (distance to layer base) was used to calculate laser beam atmospheric attenuation. Again based on radiosonde data, 0130 MST, 24 August, molecular scattering attenuation and water vapor attenuation values of 0.85 and 0.95, respectively, were obtained. The integrated water mass number for this day was 1.5 gm/cm^2. Clear-day aerosol attenuation factor was 0.64. Other computed parameters were range corrected average power received, 2.98×10^2 watts-m^2; laser output energy, 0.9 joule; and photomultiplier gain, 8.7×10^4. These numerical values yielded a volume backscattering coefficient of 3.2×10^{-5}/km.

By using the previously computed average backscattering cross-sectional area of $1.6 \times 10^{-9} m^2$ per cirrus ice crystal and the above volume backscattering coefficient, an average ice crystal density of 2×10^4 ice particles/m^3 was established for the layer of Figure 9d.

Consideration is now given to the possible existence of an arid aerosol layer since atmospheric water content at 14.3 km is usually minimal. Aerosol accumulations over the White Sands Missile Range vicinity have been reported at altitudes between 12 and 27 km [18, 19]. Dyer and Hicks [20] have reported aerosol layers in the 8 to 15 km interval with radii of 0.1μ to 1μ. Chagnon and Junge [21] had previously determined the same radius range for aerosols which consistently exhibited maximum in the lower stratosphere and found these aerosol to have a size distribution approximately inverse to the square of the particle radius. With such a size distribution, the highest concentration of particles is that for aerosols with a radius of 0.1μ.

Nonhygroscopic aerosols are the dust and metallic particles which are known to be insoluble in water. Therefore the particle's real index of refraction was considered to be near infinity. It was also assumed that these nonnucleating aerosols are spherical and nonabsorbing. For a 0.1μ to 1μ radius spherical particle with an index of refraction near infinity, and an impinging wavelength of 0.694μ, the backscattering efficiency is a maximum at a radius of 0.113μ [22]. A 0.113μ radius was found sufficiently close to the maximum aerosol concentration radius of 0.1μ to insure that its use will provide an approximation of the maximum volume backscattering coefficient within the 0.1μ to 1μ radius aerosol distribution. The choice of a particle radius near 0.1 also insured that the aerosol was nonnucleogenic since its radius of curvature is less than the critical size for which a droplet and the vapor pressure are likely to exist in equilibrium.

When a particle radius of 0.113μ was used, the backscattering cross-sectional area was $1.46 \times 10^{-13} m^2$/particle. This value was divided into the volume backscattering coefficient of 3.2×10^{-5}/m and an average aerosol concentration of 2.2×10^8 particles per m^3 was obtained. These types of striations of hard dust, quartz, and clays or metallic particles such as Al, Fe and Ti [23] present a more erosive material to reentering missiles when compared to liquid droplets, ice crystals, and their soft nuclei. The layer thickness in this case was 500 m, and again the Athena reentry angle was approximately 23°. Thus the missile traversed almost 1280 m of either ice crystals with an effective concentration of 2×10^4 particles/m^3 or the harder arid particle matter with a concentration of 2.2×10^8 particles/m^3.

CONCLUSIONS

The lidar system was successfully employed to detect conventionally undiscernible atmospheric clouds and layers along a missile reentry corridor. Such layers introduce unexpected additional nose-cone erosion which can eventually alter the projectile's angle of attack. Subvisible particulate concentrations were located at heights of 9.3 km and 14.3 km on 26 April and 24 August 1973. On each of these nights an Athena-H missile reentered the atmosphere in the vicinity of the laser probed region. These two tenuous layers were measured to be 360 m and 500 m, respectively, in vertical depth. Analysis of the lidar data, concurrently recorded radiosonde atmospheric density and relative humidity data, and an aerosol model yielded an average volume backscattering coefficient of 4.3×10^{-5}/m for 9.3 km layer and 3.2×10^{-5}/m for the 14.3 km layer. Based on previous in-situ measurements of cloud and aerosol particle sizes and shapes at the given altitudes and atmospheric

temperatures, average particle concentrations were calculated for each layer. On 26 April the cloud striations had concentrations of 3.7×10^5 liquid droplets/m^3, or 2.6×10^4 ice crystals/m^3, or a combination thereof. The higher altitude layer of 24 August had either a concentration of 2×10^4 ice particles/m^3 or 2.2×10^8 particles/m^3 of the harder arid aerosols.

Although lidar probing of the atmosphere has successfully detected clouds and aerosol layers below radar thresholds and has aided in defining a truly clear atmospheric condition during reentry missions, the data analysis of these results required that assumptions be made regarding the subvisible layer particulate sizes, shapes, and elemental composition. In this regard, this report has established an additional requirement for additional and more accurate measurements of cirrus cloud particulate size, shape, phase, and liquid to ice ratios as a function of cloud altitude and temperature. A scarcity of stratospheric aerosol microstructure measurements was also found to exist, particularly in the category of the more erosive, usually anhydrous, hard aerosols. Simultaneous lidar and in-situ measurements of the aforementioned parameters would be especially useful as a data base for future lidar support of reentry missions.

REFERENCES

1. SAMSO Technology Needs Documentation (s), Space and Missile Systems Organization, December 1974.

2. Neiger, J., private communication, Aerospace Corporation, El Segundo, California.

3. Platt, C. M. R., 1973, "Lidar and Radiometric Observations of Cirrus Clouds," Journal of Atmospheric Sciences, 30, 1191-1204.

4. Gambling, D. J., and K. Bartusek, 1972, "Lidar Observations of Tropospheric Aerosols," Atmospheric Environment, Pergamon Press, 6, 181-190.

5. Bigg, K. E., 1956, "The Detection of Atmospheric Dust and Temperature Inversions by Twilight Scattering," Journal of Meteorology, 13, 262-268.

6. Landry, M. J., and J. R. Lockner, 1968, "Laser Light Detecting and Ranging (LIDAR) Systems GB-60A and GB-60B," Sandia Laboratory Report SC-DR-67-850.

7. Jennings, D. A., "Power and Energy Measurements of Repeatively Pulsed Lasers," NBS Technical Note 398, March 1971.

8. McClatchy, R. A., R. W. Fenn, J. E. A. Selby, F. E. Volz, and J. S. Garing, "Optical Properties of the Atmosphere," (Revised) AFCRL-71-0279, May 1971.

9. Dobbins, D. L., and A. H. La Grone, 1969, "Number Density Determination in the Atmosphere of O_2, H_2O, and CO_2 Gas Constituents by Use of a High Intensity Laser Beam," Radio Science, Vol 4, No. 5, p 408.

10. Wittke, J. P., "Effects of Elevated Temperatures on the Fluorescence and Optical Maser Action of Ruby," Journal of Applied Physics, Vol 33, No. 7, pp 2333-2335.

11. Collis, R. T. H., 1962, "Lidar," Advances In Geophysics, H. E. Landsberg and J. V. Miegham, Eds., New York, Academic Press, 113-139.

12. Mason, B. J., 1971, The Physics of Clouds, Chapter 4, Oxford University Press.

13. Muller, A., and J. C. Thompson, 1970, Elements of Meteorology, Charles E. Merrill Publishing Co.

14. Van de Hulst, H. C., 1957, Light Scattering by Small Particles, John Wiley and Sons, NY.

15. Heymsfield, A. J., and L. J. Johnson, 1975, "Microstructure of Tropopause Cirrus Layers," Proceedings Sixth Conference on Aerospace and Meteorology, p 43.

16. Evan, W. E., "Remote Probing of High Cloud Via Satellite-Borne Lidar," Stanford Research Institute Final Report, August 1968, pp 88-97 (contract NASr-49(27)).

17. Schotland, R. M., K. Sassen, and R. Stone, 1971, "Observations by Lidar of Linear Depolarization Ratios for Hydrometeors," Journal of Applied Meteorology, Vol 10, No. 5, pp 1011-1017.

18. Volz, F. E., 1971, "Stratospheric Aerosol Layers from Balloon-Borne Horizon Photographs," Bulletin of the American Meteorological Society, Vol 52, No. 10, pp 996-998.

19. Miranda, A. M., Jr., and R. Fenn, 1974, Stratospheric Aerosol Sizes," Geophysical Research Letters, Vol 1, No. 5, pp 201-203.

20. Dyer, A. J., and B. B. Hicks, "Global Spread of Volcanic Dust From the Bali Eruption of 1963," Quarterly Journal of the Royal Meteorological Society, Vol 94, No. 402.

21. Chagnon, C. W., and C. E. Junge, 1961, "The Vertical Distribution of Sub-Micron Particles in the Stratosphere," Journal of Meteorology, 18, 746-752.

22. Christian, L. O., "Radar Cross Sections for Totally Reflecting Spheres," ECOM Report 5142, August 1967.

23. Farlow, N. H., G. V. Ferry, and H. Y. Lem, 1973, "Analysis of Individual Particles Collected from the Stratosphere," Cospar Space Res XIII, Fifteenth Plenary Meeting, 10-24 May 1972, Madrid, Spain.

ATMOSPHERIC SCIENCES RESEARCH PAPERS

1. Lindberg, J.D., "An Improvement to a Method for Measuring the Absorption Coefficient of Atmospheric Dust and other Strongly Absorbing Powders," ECOM-5565, July 1975.
2. Avara, Elton, P., "Mesoscale Wind Shears Derived from Thermal Winds," ECOM-5566, July 1975.
3. Gomez, Richard B. and Joseph H. Pierluissi, "Incomplete Gamma Function Approximation for King's Strong-Line Transmittance Model," ECOM-5567, July 1975.
4. Blanco, A.J. and B.F. Engebos, "Ballistic Wind Weighting Functions for Tank Projectiles," ECOM-5568, August 1975.
5. Taylor, Fredrick J., Jack Smith, and Thomas H. Pries, "Crosswind Measurements through Pattern Recognition Techniques," ECOM-5569, July 1975.
6. Walters, D.L., "Crosswind Weighting Functions for Direct-Fire Projectiles," ECOM-5570, August 1975.
7. Duncan, Louis D., "An Improved Algorithm for the Iterated Minimal Information Solution for Remote Sounding of Temperature," ECOM-5571, August 1975.
8. Robbiani, Raymond L., "Tactical Field Demonstration of Mobile Weather Radar Set AN/TPS-41 at Fort Rucker, Alabama," ECOM-5572, August 1975.
9. Miers, B., G. Blackman, D. Langer, and N. Lorimier, "Analysis of SMS/GOES Film Data," ECOM-5573, September 1975.
10. Manquero, Carlos, Louis Duncan, and Rufus Bruce, "An Indication from Satellite Measurements of Atmospheric CO_2 Variability," ECOM-5574, September 1975.
11. Petracca, Carmine and James D. Lindberg, "Installation and Operation of an Atmospheric Particulate Collector," ECOM-5575, September 1975.
12. Avara, Elton P. and George Alexander, "Empirical Investigation of Three Iterative Methods for Inverting the Radiative Transfer Equation," ECOM-5576, October 1975.
13. Alexander, George D., "A Digital Data Acquisition Interface for the SMS Direct Readout Ground Station—Concept and Preliminary Design," ECOM-5577, October 1975.
14. Cantor, Israel, "Enhancement of Point Source Thermal Radiation Under Clouds in a Nonattenuating Medium," ECOM-5578, October 1975.
15. Norton, Colburn and Glenn Hoidale, "The Diurnal Variation of Mixing Height by Month over White Sands Missile Range, NM," ECOM-5579, November 1975.
16. Avara, Elton P., "On the Spectrum Analysis of Binary Data," ECOM-5580, November 1975.
17. Taylor, Fredrick J., Thomas H. Pries, and Chao-Huan Huang, "Optimal Wind Velocity Estimation," ECOM-5581, December 1975.
18. Avara, Elton P., "Some Effects of Autocorrelated and Cross-Correlated Noise on the Analysis of Variance," ECOM-5582, December 1975.
19. Gillespie, Patti S., R.L. Armstrong, and Kenneth O. White, "The Spectral Characteristics and Atmospheric CO_2 Absorption of the Ho^{+3}:YLF Laser at 2.05μm," ECOM-5583, December 1975.
20. Novlan, David J., "An Empirical Method of Forecasting Thunderstorms for the White Sands Missile Range," ECOM-5584, February 1976.
21. Avara, Elton P., "Randomization Effects in Hypothesis Testing with Autocorrelated Noise," ECOM-5585, February 1976.
22. Watkins, Wendell R., "Improvements in Long Path Absorption Cell Measurement," ECOM-5586, March 1976.
23. Thomas, Joe, George D. Alexander, and Marvin Dubbin, "SATTEL — An Army Dedicated Meteorological Telemetry System," ECOM-5587, March 1976.
24. Kennedy, Bruce W. and Delbert Bynum, "Army User Test Program for the RDT&E-XM-75 Meteorological Rocket," ECOM-5588, April 1976.

25. Barnett, Kenneth M., "A Description of the Artillery Meteorological Comparisons at White Sands Missile Range, October 1974 — December 1974 ('PASS' — Prototype Artillery [Meteorological] Subsystem)," ECOM-5589, April 1976.
26. Miller, Walter B., "Preliminary Analysis of Fall-of-Shot From Project 'PASS'," ECOM-5590, April 1976.
27. Avara, Elton P., "Error Analysis of Minimum Information and Smith's Direct Methods for Inverting the Radiative Transfer Equation," ECOM-5591, April 1976.
28. Yee, Young P., James D. Horn, and George Alexander, "Synoptic Thermal Wind Calculations from Radiosonde Observations Over the Southwestern United States," ECOM-5592, May 1976.
29. Duncan, Louis D. and Mary Ann Seagraves, "Applications of Empirical Corrections to NOAA-4 VTPR Observations," ECOM-5593, May 1976.
30. Miers, Bruce T. and Steve Weaver, "Applications of Meterological Satellite Data to Weather Sensitive Army Operations," ECOM-5594, May 1976.
31. Sharenow, Moses, "Redesign and Improvement of Balloon ML-566," ECOM-5595, June 1976.
32. Hansen, Frank V., "The Depth of the Surface Boundary Layer," ECOM-5596, June 1976.
33. Pinnick, R.G. and E.B. Stenmark, "Response Calculations for a Commercial Light-Scattering Aerosol Counter," ECOM-5597, July 1976.
34. Mason, J. and G.B. Hoidale, "Visibility as an Estimator of Infrared Transmittance," ECOM-5598, July 1976.
35. Bruce, Rufus E., Louis D. Duncan, and Joseph H. Pierluissi, "Experimental Study of the Relationship Between Radiosonde Temperatures and Radiometric-Area Temperatures," ECOM-5599, August 1976.
36. Duncan, Louis D., "Stratospheric Wind Shear Computed from Satellite Thermal Sounder Measurements," ECOM-5800, September 1976.
37. Taylor, F., P. Mohan, P. Joseph and T. Pries, "An All Digital Automated Wind Measurement System," ECOM-5801, September 1976.
38. Bruce, Charles, "Development of Spectrophones for CW and Pulsed Radiation Sources," ECOM-5802, September 1976.
39. Duncan, Louis D. and Mary Ann Seagraves, "Another Method for Estimating Clear Column Radiances," ECOM-5803, October 1976.
40. Blanco, Abel J. and Larry E. Traylor, "Artillery Meteorological Analysis of Project Pass," ECOM-5804, October 1976.
41. Miller, Walter and Bernard Engebos, "A Mathematical Structure for Refinement of Sound Ranging Estimates," ECOM-5805, November, 1976.
42. Gillespie, James B. and James D. Lindberg, "A Method to Obtain Diffuse Reflectance Measurements from 1.0 to 3.0μm Using a Cary 17I Spectrophotometer," ECOM-5806, November 1976.
43. Rubio, Roberto and Robert O. Olsen, "A Study of the Effects of Temperature Variations on Radio Wave Absorption," ECOM-5807, November 1976.
44. Ballard, Harold N., "Temperature Measurements in the Stratosphere from Balloon-Borne Instrument Platforms, 1968-1975," ECOM-5808, December, 1976.
45. Monahan, H.H., "An Approach to the Short-Range Prediction of Early Morning Radiation Fog," ECOM-5809, January 1977.
46. Engebos, Bernard Francis, "Introduction to Multiple State Multiple Action Decision Theory and Its Relation to Mixing Structures," ECOM-5810, January 1977.
47. Low, Richard D.H., Effects of Cloud Particles on Remote Sensing from Space in the 10-Micrometer Infrared Region, ECOM-5811, January 1977.
48. Bonner, Robert S. and R. Newton, "Application of the AN/GVS-5 Laser Rangefinder to Cloud Base Height Measurements," ECOM-5812, February 1977.

49. Rubio, Roberto, "Lidar Detection of Subvisible Reentry Vehicle Erosive Atmospheric Material," ECOM-5813, March 1977.

DISTRIBUTION LIST

Commanding Officer
Picatinny Arsenal
ATTN: SARPA-TS-S, #59
Dover, NJ 07801

Commanding Officer
Harry Diamond Laboratory
ATTN: Library
2800 Powder Mill Road
Adelphi, MD 20783

Commander
US Army Electronics Command
ATTN: DRSEL-RD-D
Fort Monmouth, NJ 07703

Naval Surface Weapons Center
Code DT 21 (Ms. Greeley)
Dahlgren, VA 22448

Air Force Weapons Laboratory
ATTN: Technical Library (SUL)
Kirtland AFB, NM 87117

Director
US Army Engr Waterways Exper Sta
ATTN: Library Branch
Vicksburg, MS 39180

Commander
US Army Electronics Command
ATTN: DRSEL-CT-D
Fort Monmouth, NJ 07703

Meteorologist in Charge
Kwajalein Missile Range
PO Box 67
APO
San Francisco, CA 96555

Environmental Protection Agency
Meteorology Laboratory
Research Triangle Park, NC 27711

Chief, Technical Services Div
DCS/Aerospace Sciences
ATTN: AWS/DNTI
Scott AFB, IL 62225

Air Force Cambridge Rsch Labs
ATTN: LCH (A. S. Carten, Jr.)
Hanscom AFB
Bedford, MA 01731

Department of the Air Force
16WS/DO
Fort Monroe, VA 23651

Director
US Army Ballistic Research Lab
ATTN: DRXBR-AM
Aberdeen Proving Ground, MD 21005

Geophysics Division
Code 3250
Pacific Missile Test Center
Point Mugu, CA 93042

National Center for Atmos Res
NCAR Library
PO Box 3000
Boulder, CO 80303

William Peterson
Research Association
Utah State University, UNC 48
Logan, UT 84322

Commander
US Army Dugway Proving Ground
ATTN: MT-S
Dugway, UT 84022

Head, Rsch and Development Div (ESA-131)
Meteorological Department
Naval Weapons Engineering Support Act
Washington, DC 20374

Commander
US Army Electronics Command
ATTN: DRCDE-R
5001 Eisenhower Avenue
Alexandria, VA 22304

Marine Corps Dev & Educ Cmd
Development Center
ATTN: Cmd, Control, & Comm Div (C^3)
Quantico, VA 22134

Commander
US Army Electronics Command
ATTN: DRSEL-WL-D1
Fort Monmouth, NJ 07703

Commander
US Army Missile Command
ATTN: DRSMI-RFGA, B. W. Fowler
Redstone Arsenal, AL 35809

Dir of Dev & Engr
Defense Systems Div
ATTN: SAREA-DE-DDR
H. Tannenbaum
Edgewood Arsenal, APG, MD 21010

Mr. William A. Main
USDA Forest Service
1407 S. Harrison Road
East Lansing, MI 48823

Naval Surface Weapons Center
Technical Library and Information
Services Division
White Oak, Silver Spring, MD 20910

Dr. A. D. Belmont
Research Division
PO Box 1249
Control Data Corp
Minneapolis, MN 55440

Dir, Elec Tech and Devices Lab
US Army Electronics Command
ATTN: DRSEL-TL-D, Bldg 2700
Fort Monmouth, NJ 07703

Director
Development Center MCDEC
ATTN: Firepower Division
Quantico, VA 22134

Commander
US Army Proving Ground
ATTN: Technical Library, Bldg 2100
Yuma, AZ 85364

US Army Liaison Office
MIT-Lincoln Lab, Library A-082
PO Box 73
Lexington, MA 02173

Library-R-51-Tech Reports
Environmental Research Labs
NOAA
Boulder, CO 80302

Head, Atmospheric Research Section
National Science Foundation
1800 G. Street, NW
Washington, DC 20550

Commander
US Army Missile Command
ATTN: DRSMI-RR
Redstone Arsenal, AL 35809

Commandant
US Army Field Artillery School
ATTN: Met Division
Fort Sill, OK 73503

Meteorology Laboratory
AFCRL/LY
Hanscom AFB
Bedford, MA 01731

Commander
US Army Engineer Topographic Lab
(STINFO CENTER)
Fort Belvoir, VA 22060

Commander
US Army Missile Command
ATTN: DRSMI-RRA, Bldg 7770
Redstone Arsenal, AL 35809

Air Force Avionics Lab
ATTN: AFAL/TSR
Wright-Patterson AFB, Ohio 45433

Commander
US Army Electronics Command
ATTN: DRSEL-VL-D
Fort Monmouth, NJ 07703

Commander
USAICS
ATTN: ATSI-CTD-MS
Fort Huachuca, AZ 85613

E&R Center
Bureau of Reclamation
ATTN: Bldg 67, Code 1210
Denver, CO 80225

HQDA (DAEN-RDM/Dr. De Percin)
Forrestal Bldg
Washington, DC 20314

Commander
Air Force Weapons Laboratory
ATTN: AFWL/WE
Kirtland AFB, NM 87117

Commander
US Army Satellite Comm Agc
ATTN: DRCPM-SC-3
Fort Monmouth, NJ 07703

Commander
US Army Electronics Command
ATTN: DRSEL-MS-TI
Fort Monmouth, NJ 07703

Commander
US Army Electronics Command
ATTN: DRSEL-GG-TD
Fort Monmouth, NJ 07703

Dr. Robert Durrenberger
Dir, The Lab of Climatology
Arizona State University
Tempe, AZ 85281

Commander
Headquarters, Fort Huachuca
ATTN: Tech Ref Div
Fort Huachuca, AZ 85613

Field Artillery Consultants
1112 Becontree Drive
ATTN: COL Buntyn
Lawton, OK 73501

Commander
US Army Nuclear Agency
ATTN: ATCA-NAW
Building 12
Fort Bliss, TX 79916

Director
Atmospheric Physics & Chem Lab
Code 31, NOAA
Department of Commerce
Boulder, CO 80302

Dr. John L. Walsh
Code 5503
Navy Research Lab
Washington, DC 20375

Commander
US Army Air Defense School
ATTN: C&S Dept, MSLSCI Div
Fort Bliss, TX 79916

Director National Security Agency
ATTN: TDL (C513)
Fort George G. Meade, MD 20755

USAF EPAC/CBT (Stop 825)
ATTN: Mr. Burgmann
Scott AFB, IL 62225

Armament Dev & Test Center
ADTC (DLOSL)
Eglin AFB, Florida 32542

Commander
US Army Ballistic Rsch Labs
ATTN: DRXBR-IB
Aberdeen Proving Ground, MD 21005

Director
Naval Research Laboratory
Code 2627
Washington, DC 20375

Commander
Naval Elect Sys Cmd HQ
Code 51014
Washington, DC 20360

The Library of Congress
ATTN: Exchange & Gift Div
Washington, DC 20540
2

CO, US Army Tropic Test Center
ATTN: STETC-MO-A (Tech Lib)
APO New York 09827

Commander
Naval Electronics Lab Center
ATTN: Library
San Diego, CA 92152

Office, Asst Sec Army (R&D)
ATTN: Dep for Science & Tech
Hq, Department of the Army
Washington, DC 20310

Director
US Army Ballistic Research Lab
ATTN: DRXBR-AM, Dr. F. E. Niles
Aberdeen Proving Ground, MD 21005

Commander
Frankford Arsenal
ATTN: Library, K2400, Bldg 51-2
Philadelphia, PA 19137

Director
US Army Ballistic Research Lab
ATTN: DRXBR-XA-LB
Bldg 305
Aberdeen Proving Ground, MD 21005

Dir, US Naval Research Lab
Code 5530
Washington, DC 20375

Commander
Office of Naval Research
Code 460-M
Arlington, VA 22217

Commander
Naval Weather Service Command
Washington Navy Yard
Bldg 200, Code 304
Washington, DC 20374

Technical Processes Br
D823
Room 806, Libraries Div NOAA
8060 13th St
Silver Spring, MD 20910

The Environmental Rsch Institute of MI
ATTN: IRIA Library
PO Box 618
Ann Arbor, MI 48107

Redstone Scientific Info Center
ATTN: Chief, Documents
US Army Missile Command
Redstone Arsenal, AL 35809

Commander
Edgewood Arsenal
ATTN: SAREA-TS-L
Aberdeen Proving Ground, MD 21010

Sylvania Elec Sys Western Div
ATTN: Technical Reports Library
PO Box 205
Mountain View, CA 94040

Commander
US Army Security Agency
ATTN: IARD-OS
Arlington Hall Station
Arlington, VA 22212
2

President
US Army Field Artillery Board
Fort Sill, OK 73503

Commandant
US Army Field Artillery School
ATTN: ATSF-TA-R
Fort Sill, OK 73503

CO, USA Foreign Sci & Tech Center
ATTN: DRXST-ISI
220 7th Street, NE
Charlottesville, VA 22901

Commander, Naval Ship Sys Cmd
Technical Library, Rm 3 S-08
National Center No. 3
Washington, DC 20360

Commandant
US Army Signal School
ATTN: ATSN-CD-MS
Fort Gordon, GA 30905

Rome Air Development Center
ATTN: Documents Library
TILD (Bette Smith)
Griffiss Air Force Base, NY 13441

HQ, ESD/DRI/S-22
Hanscom AFB
MA 01731

Commander
Frankford Arsenal
ATTN: J. Helfrich PDSP 65-1
Philadelphia, PA 19137

Director
Defense Nuclear Agency
ATTN: Tech Library
Washington, DC 20305

Department of the Air Force
5WW/DOX
Langley AFB, VA 23665

Commander
US Army Missile Command
ATTN: DRSMI-RER (Mr. Haraway)
Redstone Arsenal, AL 35809

CPT Hugh Albers, Exec Sec
Interdept Committee on Atmos Sci
Fed Council for Sci & Tech
National Sci Foundation
Washington, DC 20550

US Army Research Office
ATTN: DRXRO-IP
PO Box 12211
Research Triangle Park, NC 27709

Commander
US Army Training & Doctrine Cmd
ATTN: ATCD-SC
Fort Monroe, VA 23651

Mil Assistant for Environmental Sciences
OAD (E & LS), 3D129
The Pentagon
Washington, DC 20301

Commander
Eustis Directorate
US Army Air Mobility R&D Lab
ATTN: Technical Library
Fort Eustis, VA 23604

National Weather Service
National Meteorological Center
World Weather Bldg - 5200 Auth Rd
ATTN: Mr. Quiroz
Washington, DC 20233

Commander
US Army Materiel Command
ATTN: DRCRD-SS (Mr. Andrew)
Alexandria, VA 22304

Commander
Frankford Arsenal
ATTN: SARFA-FCD-O, Bldg 201-2
Bridge & Tarcony Sts
Philadelphia, PA 19137

Inge Dirmhirn, Professor
Utah State University, UMC 48
Logan, UT 84322

Chief, Aerospace Environ Div
Code ES41
NASA
Marshall Space Flight Center, AL 35802

Dr. Frank D. Eaton
PO Box 3038
University Station
Laramie, Wyoming 82071

Commander
US Army Arctic Test Center
ATTN: STEAC-OP-PL
APO Seattle 98733

Commander
US Army Electronics Command
ATTN: DRSEL-GS-H (Stevenson)
Fort Monmouth, NJ 07703

Commander
USACACDA
ATTN: ATCA-CCC-W
Fort Leavenworth, KS 66027

Commander
US Army Test & Eval Cmd
ATTN: DRSTE-FA
Aberdeen Proving Ground, MD 21005

Air Force Cambridge Rsch Labs
ATTN: LKI
L. G. Hanscom Field
Bedford, MA 01730

Director, Systems R&D Service
Federal Aviation Administration
ATTN: ARD-54
2100 Second Street, SW
Washington, DC 20590

USAFETAC/CB (Stop 825)
Scott AFB
IL 62225

Director
USAE Waterways Experiment Station
ATTN: Library
PO Box 631
Vicksburg, MS 39180

Defense Documentation Center
ATTN: DDC-TCA
Cameron Station (BLDG 5)
Alexandria, Virginia 22314
12

Commander
US Army Electronics Command
ATTN: DRSEL-CT-S
Fort Monmouth, NJ 07703

Commander
Holloman Air Force Base
6585 TG/WE
Holloman AFB, NM 88330

Commandant
USAFAS
ATTN: ATSF-CD-MT (Mr. Farmer)
Fort Sill, OK 73503
2

Commandant
USAFAS
ATTN: ATSF-CD-C (Mr. Shelton)
Fort Sill, OK 73503
2

Commander
US Army Electronics Command
ATTN: DRSEL-CT-S (Dr. Swingle)
Fort Monmouth, NJ 07703
3

☆ U.S. GOVERNMENT PRINTING OFFICE: 1977—777-022/12